Gap Flows through Idealized Topography. Part I: Forcing by Large-Scale Winds in the Nonrotating Limit

SAŠA GABERŠEK* AND DALE R. DURRAN

Department of Atmospheric Sciences, University of Washington, Seattle, Washington

(Manuscript received 3 September 2003, in final form 26 April 2004)

ABSTRACT

Gap winds produced by a uniform airstream flowing over an isolated flat-top ridge cut by a straight narrow gap are investigated by numerical simulation. On the scale of the entire barrier, the proportion of the oncoming flow that passes through the gap is relatively independent of the nondimensional mountain height ϵ, even over that range of ϵ for which there is the previously documented transition from a ''flow over the ridge'' regime to a ''flow around'' regime.

The kinematics and dynamics of the gap flow itself were investigated by examining mass and momentum budgets for control volumes at the entrance, central, and exit regions of the gap. These analyses suggest three basic behaviors: the *linear regime* (small ϵ) in which there is essentially no enhancement of the gap flow; the *mountain wave* regime ($\epsilon \sim 1.5$) in which vertical mass and momentum fluxes play a crucial role in creating very strong winds near the exit of the gap; and the *upstream-blocking* regime ($\epsilon \sim 5$) in which lateral convergence generates the strongest winds near the entrance of the gap.

Trajectory analysis of the flow in the strongest events, the mountain wave events, confirms the importance of net subsidence in creating high wind speeds. Neglect of vertical motion in applications of Bernoulli's equation to gap flows is shown to lead to unreasonable wind speed predictions whenever the temperature at the gap exit exceeds that at the gap entrance. The distribution of the Bernoulli function on an isentropic surface shows a correspondence between regions of high Bernoulli function and high wind speeds in the gap-exit jet similar to that previously documented for shallow-water flow.

1. Introduction

Strong surface winds can develop in several ways when stably stratified air interacts with a mountain barrier. In one prototypical case—downslope windstorms—the winds blow down the lee slope of a mountain ridge. Downslope windstorms occur only when there is a significant cross-barrier flow. In a second prototypical case—gap winds—the winds blow through a gap in the ridge. Gap winds typically occur when there is a significant drop in atmospheric pressure between the entrance and exit regions of the gap. Gap winds, which have received considerably less theoretical attention than downslope winds, are the focus of this paper.

The pressure differences responsible for gap winds can be generated by several types of synoptic-scale weather patterns. Low-level cross-barrier pressure gradients may be present even when the large-scale flow surrounding the mountain is essentially stagnant provided there are significant low-level temperature differences in the air masses on each side of the mountain. Gap flow under such conditions occurs frequently during the summer in the Columbia River Gorge (between the states of Washington and Oregon in the United States). When synoptic-scale pressure gradients exist above mountain-top level they are usually in approximate geostrophic balance with the larger-scale flow. Geostrophically balanced pressure gradients associated with the large-scale flow have been identified as the primary agent in creating gap flows in locations such as the Shelikof Strait in Alaska (Lackmann and Overland 1989) and Lake Torneträsk in Scandinavia (Smedman et al. 1996) through a process known as ''pressure driven channeling'' (Whiteman and Doran 1993). Perhaps the most common type of gap flow occurs in connection with cold-air surges, when both significant cross-mountain winds and cross-mountain temperature differences may be present. Examples of this type include the wintertime easterlies in the Columbia River Gorge, as well as easterly gap winds in Howe Sound, British Columbia, (Jackson and Steyn 1994a,b), the Strait of Juan de Fuca (Overland 1984; Colle and Mass 2000), and the Strait of Gibraltar (Scorer 1952; Dorman et al. 1995), and northerly winds through Chivela Pass into the Gulf of Tehuantepec, Mexico (Steenburgh et al. 1998).

* Current affiliation: Faculty of Mathematics and Physics, University of Ljubljana, Ljubljana, Slovenia.

Corresponding author address: Dr. Dale R. Durran, Dept. of Atmospheric Sciences, University of Washington, P.O. Box 351640, Seattle, WA 98195-1640.
E-mail: durrand@atmos.washington.edu

This is the first of a pair of papers that will attempt to present a relatively comprehensive analysis of those gap flows that are dynamically forced by the interaction of a large-scale flow with the topography. The more complicated problem of gap winds driven by the combined influences of cross-mountain winds and temperature differences is left for future study.

Many previous theoretical studies of gap flow have used shallow-water theory to examine the response of flow within a channel to changes in the channel width and channel depth (Baines 1995, chapters 2 and 3). While such studies are very useful for investigating the response to small-scale features within the gap, the potential for mesoscale circulations near the gap-entrance and -exit regions to dominate the total cross-gap pressure gradient (Colman and Dierking 1992; Colle and Mass 1998a,b) provides the motivation for our approach in Part I of this paper, which is to examine the processes that occur along the entire length of the gap, including the entrance and exit regions. In particular, this paper focuses on the regimes of free-slip gap flow generated by mesoscale pressure perturbations arising from the interaction of a uniform cross-mountain flow with a mountain barrier cut by a straight, sea level gap. Coriolis forces are neglected. The influence of surface friction and the relative importance of mesoscale and geostrophically balanced synoptic-scale pressure perturbations (pressure-driven channeling) in determining the strength and structure of gap flow will be considered in Part II.

Idealized simulations of gap winds generated by a uniformly stratified airstream flowing perpendicular to the long axis of the barrier (and parallel to the axis of the gap or mountain pass) have been conducted by Saito (1993) and Zängl (2002), both of whom found that significant gap flows could develop in response to mesoscale pressure gradients produced by the large-scale cross-ridge flow. The focus in this paper is on the detailed analysis of the kinematics and dynamics that are responsible for the generation of the high gap winds that can develop in such cross-mountain flows, including

- the extent to which air is deflected through the gap or around the ends of a ridge as a function of the nondimensional mountain height,
- the variations, with respect to the nondimensional mountain height, in the portion of the gap within which the maximum flow acceleration occurs and the dynamical processes responsible for that acceleration, and
- the application of Bernoulli's theorem to those cases with the strongest gap winds.

2. Model description

The calculations presented in this paper were conducted using a numerical model to simulate nonhydrostatic compressible flow governed by the equations

$$\frac{\partial u_i}{\partial t} + u_j\frac{\partial u_i}{\partial x_j} + c_p\theta\frac{\partial \pi'}{\partial x_i} - \delta_{i3}g\frac{\theta - \overline{\theta}}{\overline{\theta}} = -\frac{1}{\rho}\frac{\partial T_{ij}}{\partial x_j}, \quad (1)$$

$$\frac{\partial \theta}{\partial t} + u_j\frac{\partial \theta}{\partial x_j} = \frac{\partial B_j}{\partial x_j}, \quad (2)$$

$$\frac{\partial \pi'}{\partial t} + \frac{R}{c_v}\frac{\partial u_j}{\partial x_j} = \frac{R\pi}{c_v\theta}\frac{\partial B_j}{\partial x_j}. \quad (3)$$

Here $(x_1, x_2, x_3) = (x, y, z)$ is the spatial position vector, $(u_1, u_2, u_3) = (u, v, w)$ is the velocity vector, θ is the potential temperature, ρ is the density, c_p and c_v are the specific heats of air at constant pressure and constant volume, and R is the gas constant for dry air. Pressure p appears in (1)–(3) through the Exner function $\pi = (p/p_0)^{R/c_p}$. The thermodynamic variables π and θ are divided such that $\pi = \overline{\pi}(z) + \pi'(x, y, z, t)$ and $\theta = \overline{\theta}(z) + \theta'(x, y, z, t)$, where the reference state $(\overline{\pi}, \overline{\theta})$ is in hydrostatic balance (i.e., $c_p\overline{\theta}\partial\overline{\pi}/\partial z = -g$). Finally, T_{ij} and B_j are the turbulent subgrid-scale fluxes of momentum and heat, parameterized in terms of an eddy diffusivity K following Lilly (1962) as

$$T_{ij} = \rho K D_{ij}, \qquad B_j = K\frac{\partial \theta}{\partial x_j}. \quad (4)$$

Here the Prandtl number has been taken as unity,

$$D_{ij} = \frac{\partial u_i}{\partial x_j} + \frac{\partial u_j}{\partial x_i} - \delta_{ij}\frac{2}{3}\frac{\partial u_l}{\partial x_l},$$

and K is proportional to $(1 - \mathrm{Ri})^{1/2}$, in which Ri is the Richardson number

$$\mathrm{Ri} = \frac{2g}{\theta}\frac{\partial \theta}{\partial x_3}\left(\sum_i\sum_j D_{ij}^2\right)^{-1/2}.$$

The numerical techniques used to solve (1)–(3) are described in Durran and Klemp (1983). The model incorporates the topography using a terrain-following coordinate (Gal-Chen and Sommerville 1975) and includes two-way interactive nesting (Skamarock and Klemp 1993). At the lateral boundaries of the coarsest grid, a one-way wave equation is applied to the normal velocity using a constant outward-directed phase speed. The linear radiation condition of Klemp and Durran (1983) and Bougeault (1983) is applied at the top boundary as modified for local evaluation by Durran (1999). At the bottom boundary, T_{13}, T_{23}, B_3, and the velocity component normal to the topography are set to zero.

The topography in our experiments is an elongated flat-topped ridge parallel to the y axis with a gap perpendicular to the ridgeline defined by the product $h(x, y) = r(x, y)g(y)$. The shape of the ridge into which the gap is incised is given by the formula

$$r(x, y) = \begin{cases} \dfrac{h_0}{16}\left[1 + \cos\left(\dfrac{\pi s}{4a}\right)\right]^4, & \text{if } s \le 4a; \\ 0, & \text{otherwise,} \end{cases} \quad (5)$$

where

$$s = \begin{cases} \max(0, |x| - b), & \text{if } |y| \le c; \\ \max\{0, [x^2 + (|y| - c)^2]^{1/2} - b\}, & \text{otherwise.} \end{cases}$$

The ridge is centered at $(x, y) = (0, 0)$ and is flat topped with uniform height h_0 over a distance $2b$ along the x axis and a distance $2(b + c)$ along the y axis. The ends of the flat-topped region are semicircular, with radius b. The slopes of the ridge have an approximate half-width a. The gap is carved out of the ridge by multiplying $r(x, y)$ by

$$g(y) = \begin{cases} 0, & \text{if } |y| \le d/2; \\ \sin\left[\dfrac{\pi(|y| - d/2)}{2e}\right], & \text{if } \dfrac{d}{2} < |y| \le e + \dfrac{d}{2}; \\ 1, & \text{otherwise.} \end{cases} \quad (6)$$

In (6), d is the width of the floor of the gap, and e is the horizontal distance over which the sidewalls rise from the floor of the gap to the ridgeline. In the simulations presented in Part I of this paper, $h_0 = 1.4$ km, $a = b = 10$ km, $c = 85$ km, $e = 5$ km, and unless otherwise noted, $d = 10$ km.

Some previous studies, both laboratory (Baines 1979) and numerical (Saito 1993), have economized by studying gap flow in a narrow channel perpendicular to the ridge axis with channel walls along the centerline of the gap and across the adjacent ridge. We also conducted simulations in such narrow domains (with slab-symmetric boundary conditions in the gap and on a section of the uniform ridge) and found a tendency for the low-level flow upstream of the gap to become blocked when Nh_0/U was large. As will be shown in sections 4 and 5, such blocking can play an important role in the dynamics of gap flow, but the physical relevance of upstream blocking in the essentially two-dimensional geometry of a channel flow is open to question. Epifanio and Durran (2001) have shown that once mountain waves begin to break, the flow over the centerline of a very long, but finite ridge is not well approximated by a purely two-dimensional simulation. In order to faithfully represent the nature of any upstream blocking (and in Part II, to accommodate large-scale winds at arbitrary angles to the ridgeline) the simulations described in this paper employ multiply nested grids to compute the flow through the gap in an isolated ridge. This configuration allows any tendency toward upstream blocking to be mitigated by the possibility of flow around each end of the ridge.

In these simulations the aspect ratio of the the ridge, defined as the length of the ridge at half height divided by the width of the ridge at half height, is $\beta = (b + c)/(a + b) = 4.75$. Epifanio and Durran (2001) found that for values of $Nh_0/U > O(1)$, the flow over the centerline of a very long ridge ($\beta = 12$) is much better approximated by that over a ridge with $\beta = 5$ than by the flow in a purely two-dimensional $(x - z)$ domain. Thus, the results reported in this paper for gaps in ridges with $\beta \sim 5$ are expected to be more representative of the flow through gaps in extremely long ridges than results obtained using the channel geometry.

Each of the nested grids covered a square domain with the gap at its center. The spatial and temporal resolution was refined by a factor of 3 on each nest. The finest grid, on which $\Delta x = 1.5$ km, occupied a square 271 km on a side, which was just large enough to include the entire mountain. The intermediate grid, on which $\Delta x = 4.5$ km, covered a square 405 km on a side. The outer grid, on which $\Delta x = 13.5$ km, extended over a square 1269 km on a side. The depth of the domain z_T was 13 km. The vertical grid spacing is variable, starting at 100 m in the layer $0 \le z \le 3$ km, then smoothly increasing to 250 m over layer $3 \le z \le 4$ km, and remaining constant at 250 m above 4 km. This vertically stretched grid allows us to efficiently resolve both the low-level gap flow and any mountain waves that might develop aloft.

The horizontal wind field is ''turned on'' instantaneously, and integrated to a nondimensional time $T \equiv Ut/a = 40$, by which point the flow in the vicinity of the topography reaches a nearly steady state. Other initialization techniques, such as a gradually ramping up of the velocity, were tested, but all approaches gave essentially the same nearly steady solution. All numerical calculations were performed with single-precision arithmetic because of computational costs. Solutions obtained using double precision differ from the single-precision simulations only in the lee of the obstacle in regions of highly turbulent flow, but there was no difference in the basic character of the quasi-steady solutions.

3. The barrier-scale response

Using linear theory, Smith (1989) investigated the development of stagnation points in flow around an isolated three-dimensional barrier. For flows with constant N and U impinging on simple convex barriers of height h_0, he noted that stagnation was favored in cases with larger values of $\epsilon = Nh_0/U$, and that in addition, the behavior of the stagnation points depended on the ratio of the cross-flow extent of the ridge to its along-flow extent β. For ridges oriented perpendicular to the flow ($\beta > 1$), stagnation is favored in the wave-breaking region above the lee slope. For ridges aligned parallel to the flow ($\beta < 1$), stagnation is favored on the windward slope in connection with the splitting and deflection of the flow around each side of the ridge. Many numerical studies have subsequently confirmed that the parameters ϵ and β are sufficient to characterize the susceptibility of cross-barrier flows with constant N and U to wave breaking and flow splitting.

When the ridge is cut by a gap, a new path becomes available along which fluid parcels may travel to the lee side of the barrier. In this section we consider two basic questions that arise when there is a gap in the topog-

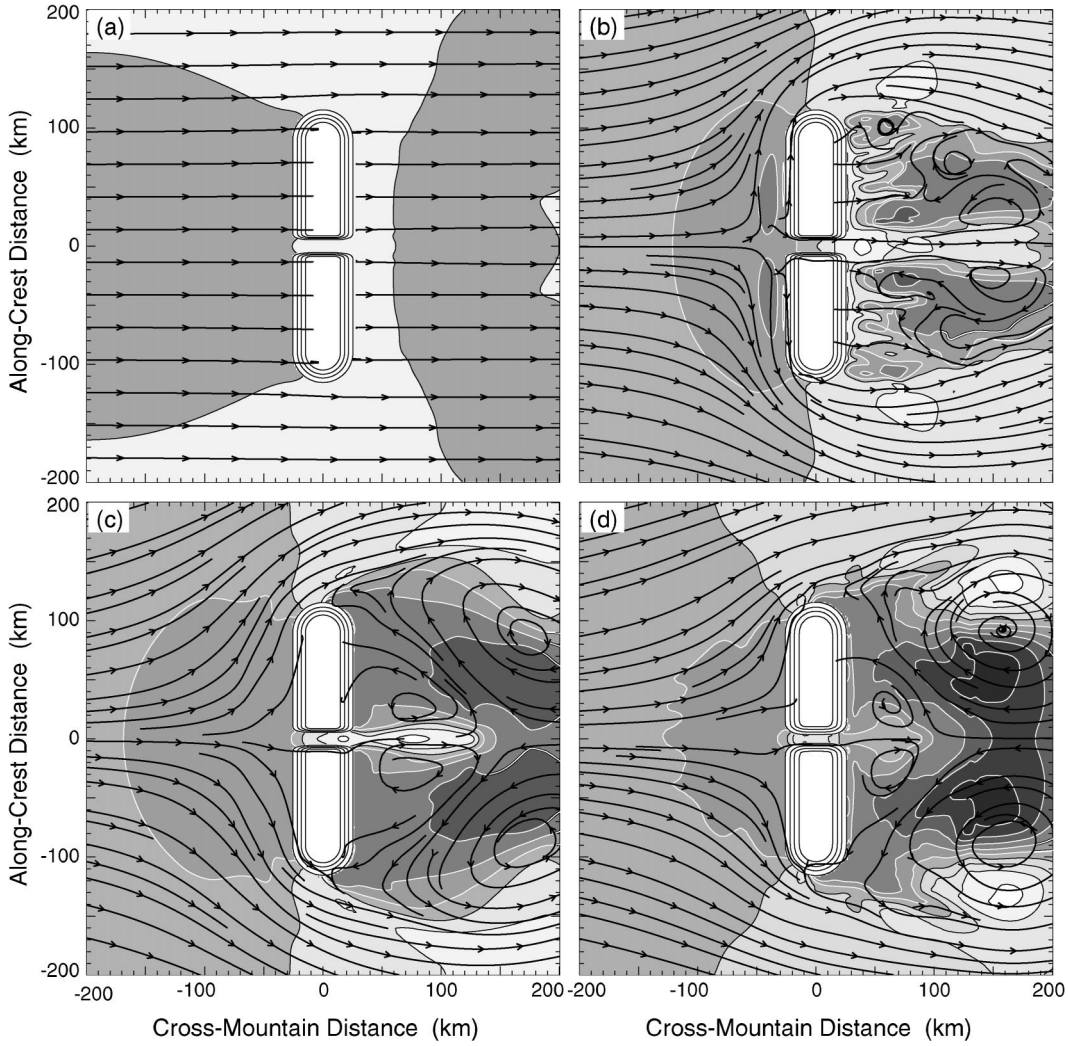

FIG. 1. Horizontal streamlines and normalized perturbation velocity $(u - U)/U$ (shaded contours) at $z = 300$ m and $T = Ut/a = 40$, for flow over a ridge with a gap when ϵ equals (a) 0.25, (b) 1.4, (c) 2.8, and (d) 5.0. The contour interval is 0.5; dark (light) shading corresponds to negative (positive) values. Terrain contours are every 300 m.

raphy. The first question is: Do the barrier-scale flow perturbations generated by a ridge with a narrow gap differ from those that develop when no gap is present? The second question is: How does the fraction of the oncoming flow that is channeled through the gap vary as a function of ϵ?

Representative examples (selected from a much larger set of simulations) of the low-level flow around ridges with and without gaps at various values of ϵ are shown in Figs. 1 and 2. The ridges were identical in all the simulations and defined according to (5). When a gap was present, it was defined by (6). The static stability was $N = 0.01\ \text{s}^{-1}$, and the variations in ϵ were achieved by changing the speed of the upstream flow, such that values of ϵ equal to (0.25, 1.4, 2.8, 5) were obtained using values of U equal to (56, 10, 5, 2.8) m s^{-1}. Each panel in Figs. 1 and 2 shows streamlines and the normalized perturbation velocity $[(u - U)/U]$ on the surface $z = 300$ m; no data are plotted where the elevation of the topography exceeds 300 m.

When $\epsilon = 0.25$ (Figs. 1a and 2a), mountain waves are present over the ridge, but there is no wave breaking and the flow is similar to that obtained for very small ϵ (not shown). The waves are clearly visible in the isentrope displacements in the vertical cross section along the gap axis plotted in Fig. 3a. Also plotted in Fig. 3 are contours of the normalized x-component perturbation velocity field using the same shading and contour intervals used in Figs. 1 and 2. For $\epsilon = 0.25$, the lateral deviation of the streamlines when they encounter the ridge or the gap is small, which is consistent with the results of Epifanio and Durran (2001), who found that only modest lateral flow deviations occurred around long uniform ridges unless the crest was high enough to trigger wave breaking over the lee slope. Figures 1a and 3a show a slight enhancement of the wind within

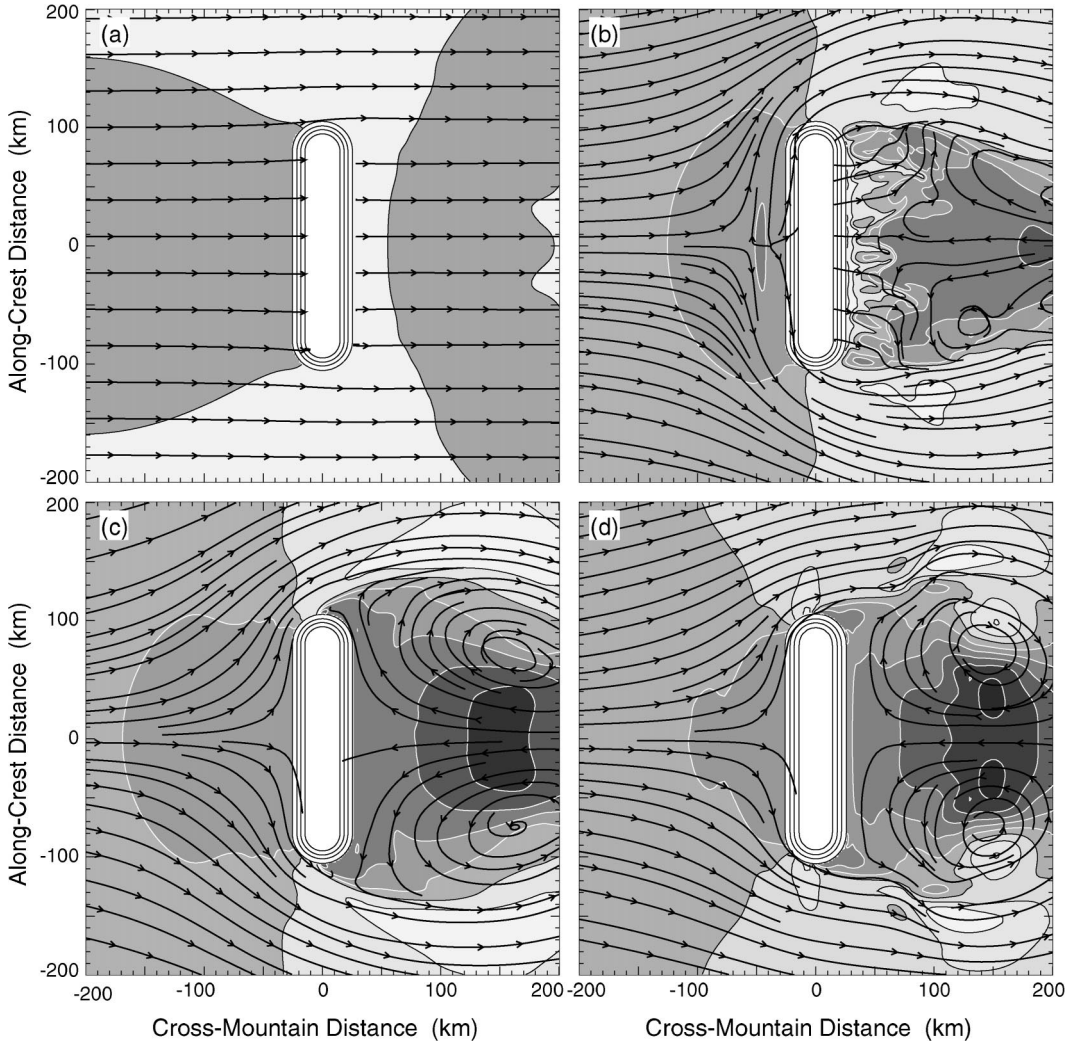

FIG. 2. Horizontal streamlines and normalized perturbation velocity, as in Fig. 1, for flow over a ridge without a gap for ϵ equal to (a) 0.25, (b) 1.4, (c) 2.8, and (d) 5.0.

and downstream of the gap, but there is no distinct jet of high winds emanating from the gap.

When $\epsilon = 1.4$ (Figs. 1b and 2b), wave breaking occurs over the lee slopes of the ridge, creating a narrow zone of high winds that ends abruptly in a feature analogous to a hydraulic jump. A turbulent wake of decelerated flow is present downstream of the jump. In the simulation without a gap the central portion of the wake contains a well-organized current of reversed flow back toward the mountain, whereas in the simulation with a gap, the wake is split by a jet flowing rapidly away from the mountain. This jet is the continuation of the accelerated gap flow, and it is flanked by a pair of vortices in which the circulation is opposite to that typically found in vortices forming in lee of a barrier without a gap. The vertical cross section along the gap axis (Fig. 3b) shows the high-amplitude wave aloft, a zone of stagnant or reversed flow (the region inside the third level of dark shading) centered near $(x, z) = (50, 1.2)$, and the extension of the gap flow well downstream from the ridge. Although the shape of the topography is somewhat different, the presence of wave breaking over the gap itself is consistent with the simulations of Zängl (2002), who in contrast to Saito (1993), found high gap winds developing beneath a wave-breaking region extending across the gap from the adjacent ridges. Upstream of the barrier, the 300-m flow is mostly blocked and deflected around the ends of the ridge. The presence of the gap enhances the upstream blocking, except in the localized region just upstream of the gap.

In comparison to the $\epsilon = 1.4$ simulations, when $\epsilon = 2.8$ the mountain waves over ridge are weaker (cf. Fig. 3c), wave breaking is reduced, and the high winds do not extend down the lee slope to the 300-m level on which the data are plotted in Figs. 1c and 2c. Downstream of the ridge without a gap, a typical pair of lee vortices produces reversed (''easterly'') flow along the centerline, but when a gap is present, a pronounced jet

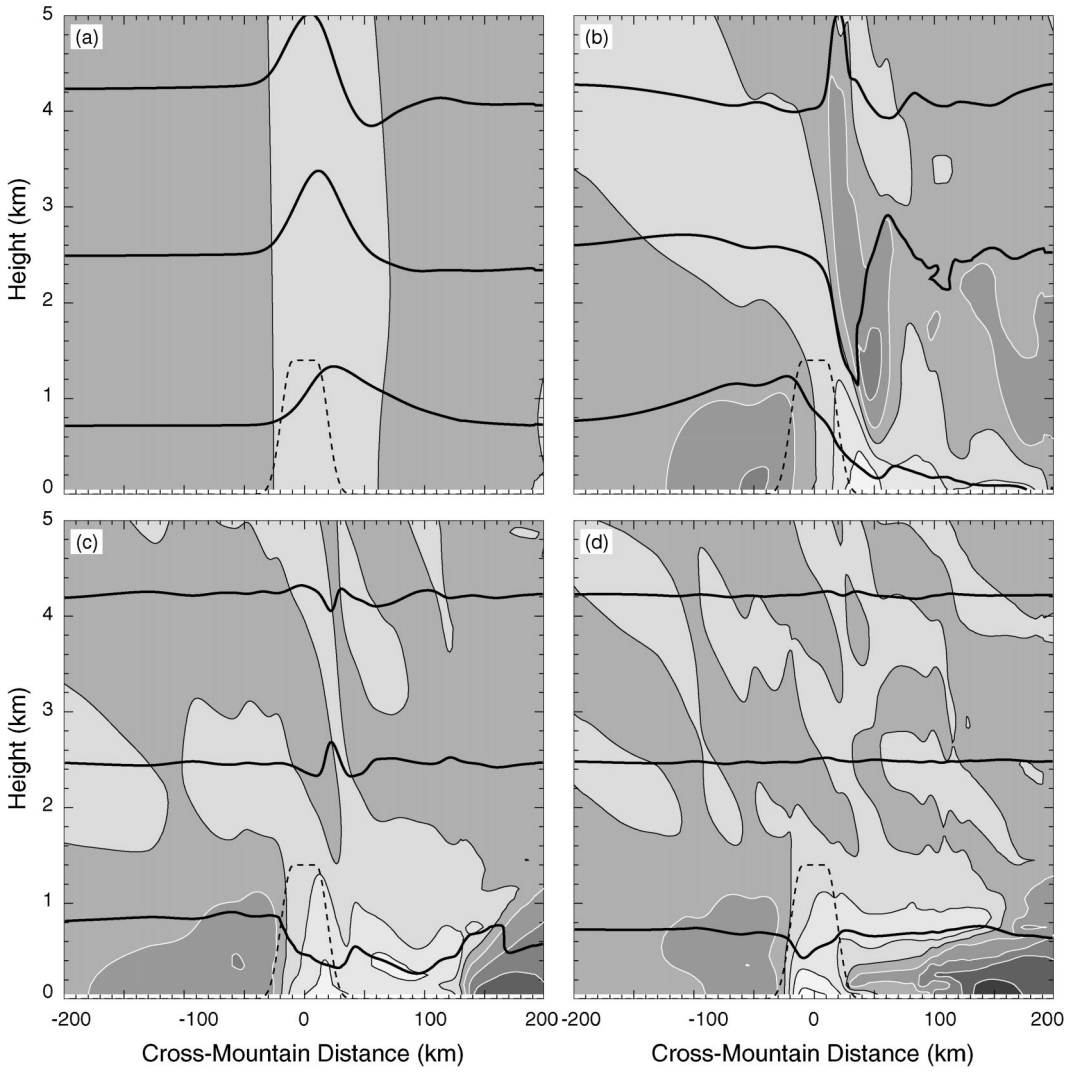

FIG. 3. Potential temperature and horizontal velocity in a *y–z* plane along the centerline of the gap for the four cases shown in Fig. 1: ϵ equal to (a) 0.25, (b) 1.4, (c) 2.8, and (d) 5.0. The heavy lines are the 275-, 280-, and 285-K isentropes; the normalized perturbation velocity field is contoured every 0.5 and shaded as in Fig. 1. The dashed line shows the profile of the adjacent ridge.

of enhanced ''westerly'' winds penetrates over 100 km downstream, splitting the wake into four distinct vortices. The gap-wind jet is flanked by a pair of smaller vortices that rotate opposite to the main pair of vortices that fill the wake farther downstream. Finally, there is slightly less deceleration immediately upstream of the central portion of the ridge when the gap is present.

The lee wave amplitude is negligible when $\epsilon = 5$ (Fig. 3d). The lee vortex patterns in the gap and no-gap simulations remain similar to those in the $\epsilon = 2.8$ case, but the jet emanating from the gap is much weaker; in fact the gap winds in the exit region are weaker than the undisturbed upstream flow (Figs. 1d and 2d). Accelerated winds are nevertheless found within the gap itself, and the lateral confluence feeding air into the gap is more pronounced than in the simulations with smaller values of ϵ.

A closer look at the flow within the gap in the preceding simulations is provided in Fig. 4, which shows the normalized pressure perturbation $[p - \overline{p}(z)]/(\epsilon\rho_0 U^2)$ at $z = 300$ m (here ρ_0 is a representative surface density), along with the normalized perturbation wind speed previously plotted in Figs. 1 and 2. Note that the region of highest perturbation wind speed shifts position as a function of ϵ. When $\epsilon = 0.25$, the normalized perturbation winds are too weak to show up at the contour interval plotted in Fig. 4; nevertheless, other plots using finer contour intervals show that the highest perturbation winds are downstream of the centerline but still within the gap. As ϵ increases to 0.5 (not shown) and 1.4, the

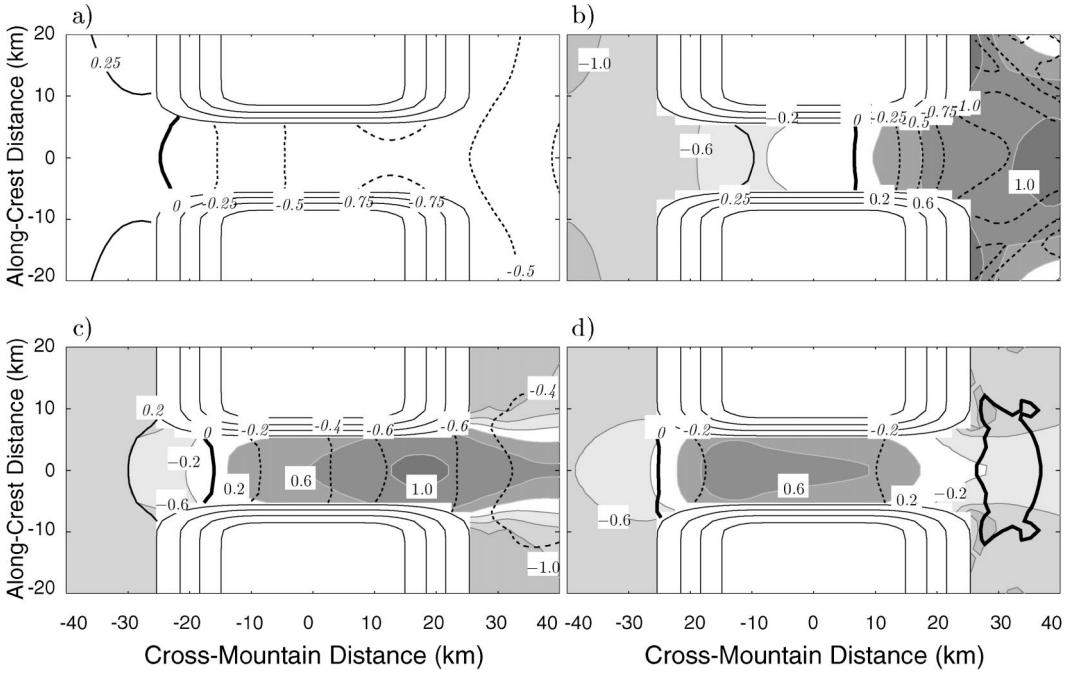

FIG. 4. Normalized pressure perturbation $(p - \overline{p})/(\epsilon\rho_0 U^2)$ (solid black lines for positive, dashed black lines for negative values, thick solid line represents zero perturbation) and normalized perturbation velocity $(u - U)/U$ (shaded contours) at $z = 300$ m and $Ut/a = 40$, for (a) $\epsilon = 0.25$, (b) $\epsilon = 1.4$, (c) $\epsilon = 2.8$, and (d) $\epsilon = 5.0$. The contour interval for pressure perturbation (italics) is 0.25 (cases $\epsilon = 0.25$ and $\epsilon = 1.4$) and 0.2 (cases $\epsilon = 2.8$ and $\epsilon = 5.0$). For velocity perturbation, the contour interval is 0.4, dark (light) shading corresponds to positive (negative) values, speeds in the interval $[-0.2, 0.2]$ are not shaded. Terrain contours are every 300 m.

normalized perturbation wind maxima strengthen and shift completely downstream of the ridge. Further increases in ϵ move the perturbation maximum wind speed back upstream; it appears back inside the gap when $\epsilon = 2.8$, and it shifts even farther upstream, to the gap-entrance region, when $\epsilon = 5.0$. The locations of the maximum wind speed perturbations are approximately coincident with the locations of the maximum wind speed perturbations are approximately coincident with the locations of the minima in the 300-m pressure field. Note that for most values of ϵ, the pressure within the gap is lower than the ambient pressure upstream; however when $\epsilon = 1.4$, the pressure in the upstream half of the gap is higher than the pressure upstream, and the pressure gradient contributing to the acceleration of the gap flow is concentrated in the gap-exit region.

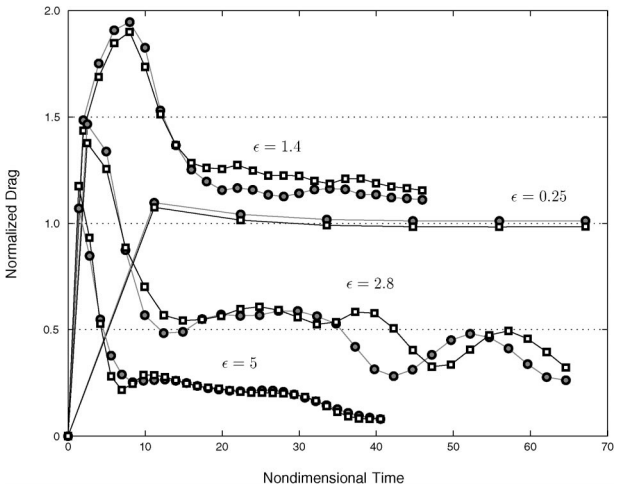

FIG. 5. Cross-mountain pressure drag D as a function of Ut/a for the simulations shown in Figs. 1 and 2. Pairs of curves are plotted for each value of ϵ, using filled circles for cases with a continuous ridge and open squares for cases with a gap.

The normalized x component of the pressure drag on the topography,

$$D = \frac{1}{\rho_0 NUh_0^2 L_y} \int_{-\infty}^{\infty} p' \frac{\partial h}{\partial x}\, dx\, dy,$$

for each of the preceding simulations is plotted as a function of nondimensional time Ut/a in Fig. 5. Here p' is the perturbation pressure and L_y is the length of the ridge, taken as $2(b + c) = 190$ km [see (5)]. The normalization factor is a scale for the pressure drag associated with linear flow over a ridge of height h_0 and length L_y, but it is not the precise drag for linear flow over the flat-top ridge defined by (5). Data for simulations with and without a gap are indicated by open squares or filled circles, respectively. The normalized drag in the weakly nonlinear $\epsilon = 0.25$ cases becomes quite steady at values of about unity after $Ut/a = 20$,

with the drag slightly stronger in the case with no gap. The slight decrease in drag when the gap is present is due to the reduction in the total area of the obstacle on which the pressure drag can act.

In contrast to previous results for pressure drag across ridges with well-defined peaks (Ólafsson and Bougeault 1997; Epifanio and Durran 2001), the maximum value of the normalized drag for the flat-top ridge is achieved at relatively small ϵ, for example, among our simulations with ϵ in the set {0.25, 0.5, 1.0}, the largest value, $D = 2.0$, was obtained for $\epsilon = 0.5$. As suggested by the remaining pairs of curves in Fig. 5, in the more nonlinear cases, the drag undergoes a strong initial transient and then settles down but never becomes completely steady. The $\epsilon = 1.4$ cases become quasi-steady with values of D around 1.1, with slightly higher drag for the ridge pierced by the gap. As noted previously, the simulation with the gap produces a little more upstream blocking along the ridges on each side of the gap, and it is the upstream pressure perturbations associated with this blocking that appear to be responsible for the slightly enhanced drag. In the $\epsilon = 5.0$ case, the drag is much weaker; it is virtually independent of the presence of the gap, and it decreases gradually in association with a long time-scale evolution of the wake. The $\epsilon = 2.8$ cases exhibit the most complex behavior. After achieving an almost steady value of 0.55 between $Ut/a = 15$ and 35, the drag begins to undergo fluctuations with a period of roughly 20 Ut/a. These fluctuations are associated with vacillations in the lee wave and wake structure that are a subject of continued investigation. The phase/onset time of the oscillation is sensitive to the presence or absence of the gap.

Now consider the question of how the fraction of the oncoming flow channeled through the gap varies as a function of ϵ. A quantitative measure of low-level flow deflection through the gap or around the ends of the ridge can be obtained by evaluating the mass fluxes through the sides of the control volume shown in Fig. 6. The lower boundary of the control volume follows the terrain, the sides are vertical planes and the top boundary follows a surface of constant potential temperature ($\theta_t = 277$ K). The downstream boundary is parallel to the y axis and is located where the topography first rises to its full height, at $x = -b = -10$ km. The downstream boundary is sufficiently upstream, with respect to the centerline of the ridge, that wave breaking never occurs within the control volume; therefore the flow along the top of the control volume is isentropic. The lateral sides are parallel to the x axis, intersecting the north and south ends of the uniform section of the ridge at $y = \pm c = \pm 85$ km. The upstream boundary is placed at $x = x_i = -200$ km, which is sufficiently far upstream to ensure that all significant deflection of the flow around the ends of the mountain is included in the mass fluxes through the lateral sides of the control volume. The mass flux budget is evaluated at nondimensional time $T = 40$, at which point the flow through the control volume in each simulation is almost completely steady.

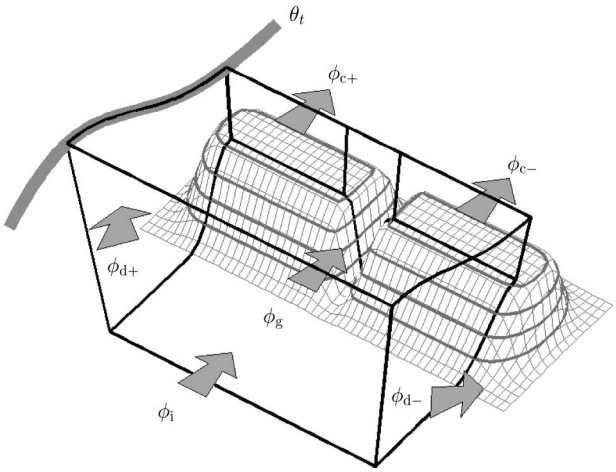

FIG. 6. A control volume for low-level mass-flux calculations.

Since at steady state, both the lower and upper boundaries of the control volume act as material surfaces, the mass entering the control volume through its upstream face is either deflected laterally around the ends of the obstacle, lifted over the ridge crest, or channeled through the gap. Let $z_t(x, y)$ be the height of the θ_t isentropic surface. The fluxes through each face of the control volume shown in Fig. 6 may be evaluated as

$$\phi_i = \int_{-c}^{c} \int_{0}^{z_t(x_i,y)} \rho u(x_i, y, z)\, dy\, dz,$$

$$\phi_{d+} = \int_{x_i}^{0} \int_{h(x,c)}^{z_t(x,c)} \rho v(x, c, z)\, dx\, dz,$$

$$\phi_{d-} = -\int_{x_i}^{0} \int_{h(x,-c)}^{z_t(x,-c)} \rho v(x, -c, z)\, dx\, dz,$$

$$\phi_{c+} = \int_{e+d/2}^{c} \int_{h_0}^{z_t(-b,y)} \rho u(-b, y, z)\, dy\, dz,$$

$$\phi_{c-} = \int_{-c}^{-e-d/2} \int_{h_0}^{z_t(-b,y)} \rho u(-b, y, z)\, dy\, dz,$$

$$\phi_g = \int_{-e-d/2}^{e+d/2} \int_{h(-b,y)}^{z_t(-b,y)} \rho u(-b, y, z)\, dy\, dz.$$

Normalized fluxes may now be defined representing the fraction of the mass entering the control volume that is deflected around the ends of the ridge $\Phi_d = (\phi_{d+} + \phi_{d-})/\phi_i$, lifted over the crest $\Phi_c = (\phi_{c+} + \phi_{c-})/\phi_i$ or channeled through the gap $\Phi_g = \phi_g/\phi_i$. These normalized mass fluxes are plotted as a function of ϵ in Fig. 7a, which clearly shows the expected shift between a flow-over regime at small ϵ and a flow-around regime at large ϵ. Somewhat surprisingly, the fraction of the

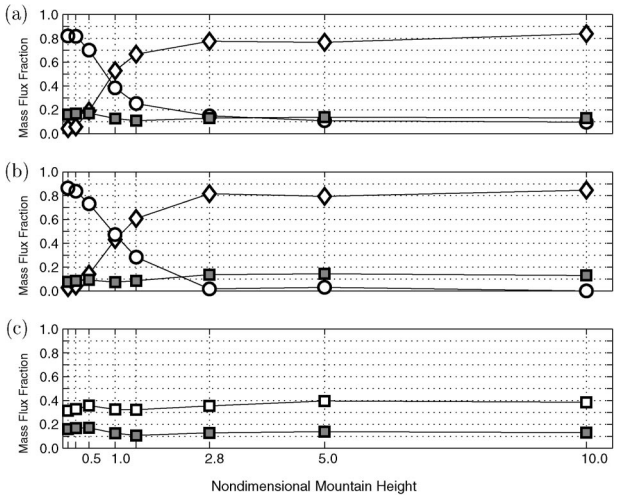

FIG. 7. Partitioning of the low-level mass flux as a function of ϵ. (a) Laterally deflected flux Φ_d (diamonds), gap flow Φ_g (shaded squares), and cross-crest flow Φ_c (circles) for the control volume shown in Fig. 6 when the bottom of the gap d is 10 km wide. (b) As in (a), except that the control volume is topped by a horizontal plane at the elevation of the ridge crest and the circles represent the vertical flux through this plane. (c) Comparison of Φ_g for $d = 10$ km (shaded squares) and $d = 40$ km (open squares).

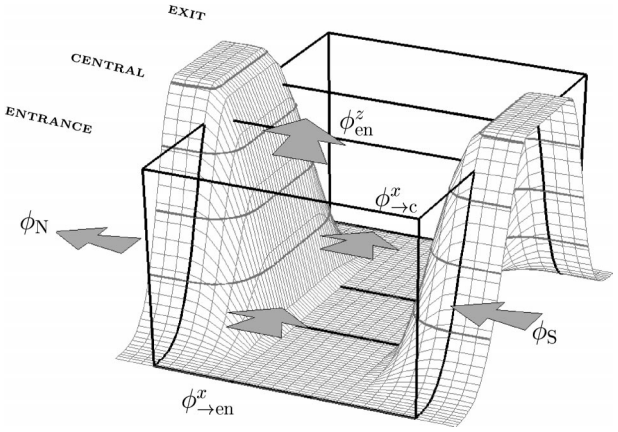

FIG. 8. Control volumes for analysis of the low-level mass budget in the gap. Arrows representing mass fluxes for the entrance region are also shown.

total mass flux that exits through the gap Φ_g is relatively independent of ϵ. For the topography shown in Fig. 1, the gap flow Φ_g varies from 0.18 to a minimum of 0.11 at $\epsilon = 1.4$ and then gradually increases back to 0.14. In contrast, over the same range of ϵ both the portion the flow deviating laterally around the ends of the ridge Φ_d and that flowing over the crest Φ_c change by roughly 100% as the flow-over regime (small ϵ) gives way to the flow-around regime (large ϵ).

The preceding analysis does not uniquely differentiate between the gap flow itself and the air that passes over the gap above the height of the ridge. Does the percentage of air passing through the gap itself exhibit a greater dependence on ϵ? To address this question, the top of the control volume defined in Fig. 6 was replaced with a horizontal plane at the height of the ridge crest, and the portion of the flow passing over the ridge was redefined as the vertical flux through this horizontal plane normalized by the total incoming flux upstream. The variation of these ''below crest'' fluxes as a function of ϵ is plotted in Fig. 7b, which shows the same basic behavior revealed in the previous analysis: as ϵ increases, there is a clear shift between a flow-over regime to a flow-around regime while the percentage of flow passing through the gap remains relatively constant. One minor piece of additional information available in Fig. 7b is that the net vertical flux through the top of the volume drops almost to zero for $\epsilon \geq 2.8$.

The robustness of the result that Φ_g does not experience a regime change as a function ϵ was verified in a second series of simulations in which the width of the bottom of the gap d was increased from 10 to 40 km [see (6)] without modifying any of the other parameters defining the shape of the topography. This increase in d widens the total y–z cross section of the gap by a factor of 2.8. The fraction of the incoming mass flux that is channeled through the gap in both the $d = 10$ and $d = 40$ km simulations is plotted as a function of ϵ in Fig. 7c. In both cases, the fraction of the flow that passes through the gap is relatively independent of ϵ. Not surprisingly, the fraction of the total flow channeled through the gap increases as the width of the gap increases. Furthermore, for a given value of ϵ, the ratio of Φ_g for the $d = 40$ km case to that in the $d = 10$ case is approximately equal to the ratio of the cross-sectional areas of the gaps in the two simulations.

4. Flow through the gap: Kinematics

Having examined the barrier-scale response, let us now consider the kinematics of the gap flow itself, which may be revealed by analyzing the mass fluxes through the series of three control volumes oriented along the gap shown in Fig. 8. The top of all three volumes is bounded by the horizontal plane $z = 1200$ m, which lies 200 m below the ridgetop. The width of each volume is the minimum of either 20 km [$d + 2e$ as defined in connection with (6)] or the actual width of the gap. The entrance volume occupies the region $-40 \leq x \leq -10$ km along the windward slopes of the ridge, the exit volume is aligned with the lee slopes over the interval $10 \leq x \leq 40$ km, and the central volume is found where the gap width is independent of x in the interval $-10 = -b \leq x \leq b = 10$ km.

Define the area-integrated mass fluxes $\phi^x_{\rightarrow {\rm en}}$, $\phi^x_{\rightarrow c}$, $\phi^x_{c\rightarrow}$, and $\phi^x_{{\rm ex}\rightarrow}$ as the integral of ρu over the y–z surfaces that constitute the upstream sides of the entrance, central and exit volumes, and the downstream face of the exit volume, respectively. Let $\phi^z_{\rm en}$, ϕ^z_c, and $\phi^z_{\rm ex}$ be the integral of ρw over x–y surfaces at the top of the entrance, central, and exit volumes. Finally, let $\phi^y_{\rm en}$ and $\phi^y_{\rm ex}$ be the

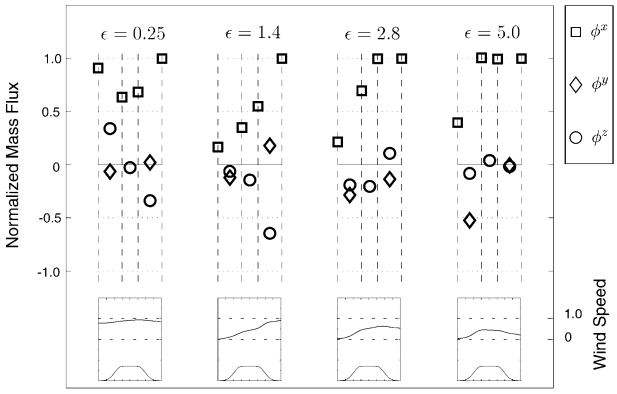

FIG. 9. Normalized mass fluxes through the control volumes shown in Fig. 8, for simulations with different ϵ. Vertical dashed lines denote the x-coordinate locations of the boundaries of the individual control volumes. For each simulation, the leftmost pair of lines delimits the entrance volume, the center pair the central volume, and the rightmost pair the exit volume. The cross-ridge topographic profile associated with these control volumes is plotted below each set of mass-flux data, along with the normalized surface wind speed. Squares, diamonds, and circles denote the normalized values of ϕ^x, ϕ^y, and ϕ^z, respectively.

net area-averaged lateral mass flux out of the entrance and exit volumes, defined for example for the entrance volume such that $\phi^y_{\text{en}} = \phi_{\text{N}} - \phi_{\text{S}}$, where ϕ_{N} and ϕ_{S} are the integrals of ρv over the ''northern'' and ''southern'' faces indicated in Fig. 8. At steady state, conservation of mass requires

$$\phi^x_{\to c} = \phi^x_{\to \text{en}} - \phi^z_{\text{en}} - \phi^y_{\text{en}}, \tag{7}$$

$$\phi^x_{c\to} = \phi^x_{\to c} - \phi^z_{c}, \tag{8}$$

$$\phi^x_{\text{ex}\to} = \phi^x_{c\to} - \phi^z_{\text{ex}} - \phi^y_{\text{ex}}. \tag{9}$$

Note that the sidewalls of the gap prevent any lateral mass fluxes from entering the central volume, and they reduce the x–y cross-sectional area of the central volume by a factor of 0.64 relative to the area of the upstream face of the entrance volume (and the downstream face to the exit volume).

The steady-state mass balance for four simulations with $\epsilon = 0.25$, 1.4, 2.8, and 5.0 is displayed in Fig. 9. In all cases the mass budget closes to within 5% of the largest term. For each simulation all terms appearing in (7)–(9) are normalized by division by $\max(|\phi^x_{\to \text{en}}|, |\phi^x_{\to c}|, |\phi^x_{c\to}|, |\phi^x_{\text{ex}\to}|)$ and plotted at representative locations along the x axis. The along-gap fluxes ϕ^x are plotted at the x coordinate of the y–z face through which the flux is transmitted, whereas the fluxes ϕ^y and ϕ^z are plotted at the x coordinate of the center of the surface through which they are transmitted. The ridge profile and the normalized *surface* wind speed $u(x, 0, 50)/[U(1 + \epsilon)]$ are also displayed for each simulation. Three basic regimes of mass transport through the gap are apparent in Fig. 9.

In the first regime, which applies to the case $\epsilon = 0.25$, the air flows up and over the topography with only minimal lateral divergence; there is no wave breaking and almost no amplification of the gap flow. The variation in the average along-gap wind speed can be deduced from the along-gap mass fluxes in this case as follows. The mass flux out the downstream face of the entrance volume $\phi^x_{\to c}$ is decreased from the upstream value $\phi^x_{\to \text{en}}$ by almost the full factor of 0.64 by which the cross-sectional area of flow is reduced within the gap. The decrease in mass flux is slightly less than 64% because there is a slight acceleration of the along-gap wind component within the entrance volume. The mass balance required by (7) is achieved primarily by removing mass through the top boundary of the entrance volume ($\phi^z_{\text{en}} > 0$); lateral convergence provides only a small contribution to the total mass balance. Within the central volume there is very slight acceleration of the flow and enhancement of the along-gap flux $\phi^x_{c\to}$ due to a weak downward flux ϕ^z_c. The mass flux out exit volume $\phi^x_{\text{ex}\to}$ is increased relative to $\phi^x_{c\to}$ by downward fluxes through the top of the exit volume ($\phi^z_{\text{ex}} < 0$); lateral divergence out the sides of the exit volume is weak. The increase in $\phi^x_{\text{ex}\to}$ relative to $\phi^x_{c\to}$ is due almost entirely to the increase in cross-sectional area of the exit volume downstream of the gap. Since $\phi^x_{\text{ex}\to}$ is only slightly greater than $\phi^x_{\to \text{en}}$, there is almost no net enhancement of the along-gap wind speed.

The second gap-flow regime, which will be called the *mountain wave regime*, is illustrated by the $\epsilon = 1.4$ case; it is characterized by a monotone increase in mass flux through each of the control volumes leading to a significant enhancement of the gap wind. Despite the reduction in the y–z cross-sectional area across the entrance volume, $\phi^x_{\to c}$ exceeds $\phi^x_{\to \text{en}}$ due to both lateral convergence ($\phi^y_{\text{en}} < 0$) and downward transport ($\phi^z_{\text{en}} < 0$). Downward mass fluxes into the central volume produce a further enhancement of $\phi^x_{c\to}$ relative to $\phi^x_{\to c}$. Finally, very strong downward fluxes in the exit region offset modest lateral divergence to accelerate the along-gap flow to the point where $\phi^x_{\text{ex}\to}$ exceeds $\phi^x_{\to \text{en}}$ by roughly a factor of 5.

A third gap-flow regime, the *upstream-blocking regime* is apparent in the $\epsilon = 5.0$ simulation, in which the largest increase in the along-gap mass flux occurs in the entrance volume due primarily to strong lateral convergence. Modest downward transport also plays a role in increasing $\phi^x_{\to c}$, but there is little subsequent change in the along-gap mass flux through central and exit regions. Since $\phi^x_{\text{ex}\to} \approx \phi^x_{c\to}$ despite the factor of 1.6 increase in the cross-sectional area between the upstream and downstream faces of the exit volume, the average wind speed decreases within the exit volume.

The behavior of the averaged along-gap wind speed deduced from the preceding mass budgets is reflected in the distributions of normalized 50-m wind speed shown at the bottom of Fig. 9. These wind speeds, taken from the lowest grid level in the numerical simulation, are normalized by $U(1 + \epsilon)$, which is a characteristic scale for the maximum horizontal wind speed that would

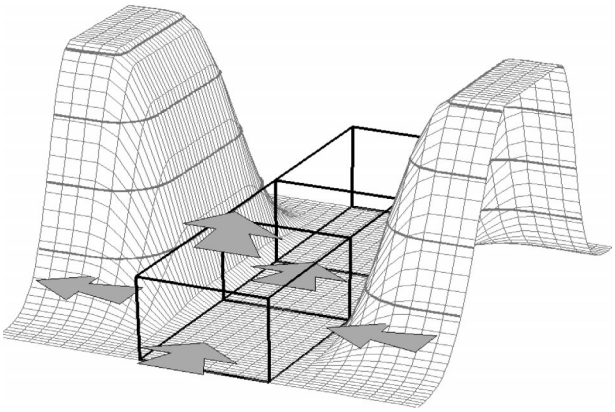

FIG. 10. Control volumes for analysis of the low-level momentum budget within the gap. Arrows representing advection through the faces of the entrance volume are also shown.

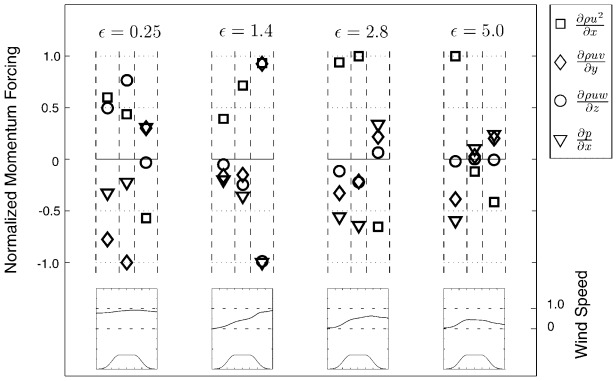

FIG. 11. Normalized momentum forcing in the control volumes shown in Fig. 10, for simulations with different ϵ. Vertical dashed lines denote the x-coordinate locations of the boundaries of the individual control volumes. For each simulation, the leftmost pair of lines delimits the entrance volume, the center pair the central volume, and the rightmost pair the exit volume. The cross-ridge topographic profile associated with these control volumes is plotted below each set of mass-flux data, along with the normalized surface wind speed. Squares, diamonds, circles, and triangles denote the normalized volume integrals of $\partial\rho u^2/\partial x$, $\partial\rho uv/\partial y$, $\partial\rho uw/\partial z$, and $\partial p/\partial x$, respectively.

be obtained in the linear mountain wave solution. Although the flow in the $\epsilon = 0.25$ case is almost linear, the surface winds within the gap itself are weaker than the maximum winds in the mountain wave aloft, and $[u(x, 0{,}50)/U](1 + \epsilon)^{-1}$ remains approximately equal to $(1 + \epsilon)^{-1}$. In particular, there is neither significant blocking near the gap entrance, nor significant acceleration of the surface winds within the gap. In contrast, upstream blocking reduces the normalized surface wind to near zero in the three cases with larger values of ϵ, and there is significant subsequent acceleration of the winds farther along the gap. In the mountain wave regime ($\epsilon = 1.4$) this acceleration occurs along the entire length of the gap and is strongest in the exit region. In the upstream-blocking regime ($\epsilon = 5.0$), acceleration occurs only in the entrance region, and the flow decelerates as it passes through the exit region. The simulation with $\epsilon = 2.8$ is an intermediate case with characteristics of both the mountain wave and upstream blocking: the flow accelerates rapidly near the gap entrance, but continued acceleration occurs through the central region of the gap to balance a downward mass flux ϕ_c^z.

5. Flow through the gap: Dynamics

The mass budgets calculated in section 4 provide information about the basic kinematics of the flow through the gap. Insight into the gap-flow dynamics can be obtained by examining the momentum budgets for three control volumes placed along the axis of gap as shown in Fig. 10. These control volumes are similar to those used in the mass-budget analysis except the cross-flow dimension of each volume was reduced to the 10-km-wide region $|y| \le d/2$ along which the bottom of the gap is completely flat, and the top of each volume was lowered to $z = 500$ m to focus on flow near the surface.

At steady state the x-momentum equation may be written in flux form as

$$\frac{\partial \rho u^2}{\partial x} + \frac{\partial \rho uv}{\partial y} + \frac{\partial \rho uw}{\partial z} + \frac{\partial p}{\partial x} = 0, \qquad (10)$$

where the divergence of the subgrid-scale fluxes has been neglected because it is negligible in comparison to the other retained terms. (These are free-slip simulations and any wave-breaking regions lie outside these control volumes). The momentum budgets for a series of simulations with different ϵ were computed once the flow in the gap reached an essentially steady state by integrating each of the terms in (10) over the three subvolumes shown in Fig. 10. Because of the flux form of (10) these volume integrals reduce to differences in the advective momentum fluxes through opposing faces, or differences in the pressure on the opposing faces of each control volume. In all cases the momentum budget obtained from this procedure closes to within 10% of the largest individual term.[1]

Each term in the volume integral of (10) is plotted in Fig. 11 for a series of simulations with $\epsilon = 0.25$, 1.4, 2.8, and 5.0. The dimensional integrals from each simulation are normalized to fall in the interval $[-1, 1]$ by dividing them by the magnitude of the largest individual integral from that simulation. These normalized results are plotted at the x coordinate of the centroid of their respective volumes (i.e., the centroids of the entrance, central, or exit regions). The topography and normalized surface wind speed $u(x, 0{,}50)/[U(1 + \epsilon)]$ are also plotted below the momentum budget data for each simulation

[1] The sole exception occurs in the exit volume of the $\epsilon = 1.4$ simulation, in which the residual is 14.6% of the largest term because of transience due to wave breaking. Nevertheless, the interpretation of the budget remains clear cut because in this case the residual is only about 15% of *all* the individual terms in the budget.

as a reference. The volume integral of $\partial\rho u^2/\partial x$ is denoted by a square, with positive values indicating net acceleration along the gap axis. Negative values of the remaining volume integrals indicate a contribution toward acceleration along the gap axis; they are the integrals of of $\partial\rho uv/\partial y$ (lateral-momentum divergence), denoted by diamonds; $\partial\rho uw/\partial z$ (vertical-momentum divergence), denoted by circles; and $\partial p/\partial x$ (pressure gradient), denoted by triangles.

As noted in the previous analysis of mass fluxes, there is little amplification of the gap flow in the $\epsilon = 0.25$ simulation. The volume-averaged acceleration in the entrance region is almost exactly offset by deceleration in the exit region; although there is also a contribution toward acceleration in the central region that produces a modest net increase in the along-gap winds. Perhaps the most interesting aspect of the momentum budget in the $\epsilon = 0.25$ case is the relative unimportance of the pressure gradient force, particularly in the entrance and central regions.

The momentum budget in the $\epsilon = 1.4$ simulation, the mountain wave regime, shows acceleration of the along-gap winds in all three subvolumes, with the rate of acceleration increasing downstream. Vertical and lateral momentum flux convergence and pressure gradient forces all contribute toward the acceleration of the flow in the entrance and central regions. Lateral momentum flux divergence acts to reduce the acceleration in the exit volume, but it is more than offset by strong pressure gradient forces and strong downward momentum transport. The mountain wave regime is the only case in which a net acceleration of the gap wind occurs within the exit region, and that acceleration is quite intense.

In contrast to the mountain wave regime ($\epsilon = 1.4$), in which vertical momentum flux convergence plays a crucial role in amplifying the gap winds, vertical momentum transport is essentially zero in the upstream-blocking regime ($\epsilon = 5.0$). Lateral momentum flux convergence and pressure gradient forces accelerate the gap flow in the entrance region and retard the flow in the exit region. The $\epsilon = 2.8$ simulation once again appears as a hybrid between the two gap-wind regimes. The momentum budgets in the entrance and exit volumes are similar to those in the upstream-blocking regime, whereas downward and lateral momentum fluxes together with the pressure gradient force produce significant accelerations within the central volume.

6. Flow through the gap: Trajectories and Bernoulli's equation

It has often been suggested that to a first approximation the dynamics of gap flow may be interpreted as a rough balance between the along-gap pressure gradient, along-gap accelerations, and surface friction (Mass et al. 1995, and references therein). The influence of surface friction will be discussed in Part II; as a preliminary step in the assessment of the preceding gap-flow paradigm, we consider the free-slip case, which is often analyzed using Bernoulli's equation (Reed 1981). Under the assumption that the air parcel trajectories are horizontal and that the vertical and cross-gap wind components are negligible, Bernoulli's equation for incompressible flow through a gap parallel to the x axis becomes

$$\frac{u_{\text{ex}}^2}{2} = \frac{u_{\text{en}}^2}{2} + \frac{p_{\text{en}} - p_{\text{ex}}}{\rho}, \tag{11}$$

where the subscripts ''en'' and ''ex'' denote quantities sampled at the gap-entrance and -exit regions, respectively. As noted by Mass et al. (1995), (11) typically overpredicts the actual acceleration experienced by air parcels passing through the gap.

It does not seem to have been recognized that a correct application of the compressible Bernoulli equation actually leads to a rather different relation for horizontal flow through a gap. Accounting for the compressibility of the atmosphere, Bernoulli's equation implies that

$$B = c_p T + \frac{1}{2} u_i u_i + gz$$

is conserved following a fluid parcel in a steady inviscid flow. Here $c_p T = c_v T + p/\rho$, and c_p and c_v are the specific heats of air at constant pressure and constant volume. As in the approximations leading to (11), suppose the flow is level and that all velocity perturbations are dominated by the component of the flow along the gap, then conservation of B implies

$$\frac{u_{\text{ex}}^2}{2} = \frac{u_{\text{en}}^2}{2} + c_p(T_{\text{en}} - T_{\text{ex}}). \tag{12}$$

It follows that *for purely horizontal flows, the gap winds in the exit region can only exceed those in the entrance region when the temperature at the exit is colder than the temperature upstream.* Since $O(c_p T) \gg O(u^2)$ the decrease in temperature required to produce a significant increase in wind speed is only a fraction of a degree; however, observations of flows through essentially level gaps often show the temperature *increases* between the entrance and exit regions.

The key element for the correct application of Bernoulli's equation to the strongest gap-wind simulations in this paper is the inclusion of vertical motion. The strongest gap winds occur in the $\epsilon = 1.4$ simulations, in which the 10 m s^{-1} upstream flow accelerates to 22 m s^{-1}. In comparison the winds in the upstream-blocking regime ($\epsilon = 5.0$) increase from 2.8 m s^{-1} upstream to 7 m s^{-1} within the gap. Consistent with the factors that produce different flow regimes over a specific mountain range in the real world, the 1.4-km height of the ridge was held fixed between the different simulations, and the values of ϵ characteristic of the flow-blocking regime were associated with relatively weak upstream winds. Thus, although the gap-induced normalized velocity perturbations $u[U(1 + \epsilon)]^{-1}$ have sim-

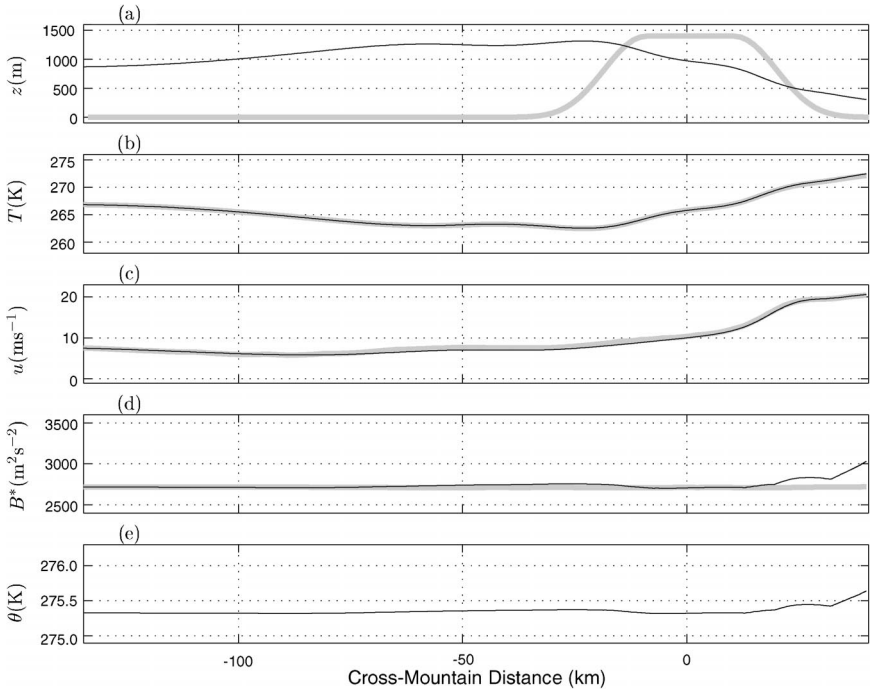

FIG. 12. Variation of key parameters along a trajectory above the centerline of the gap that exits at the height $z = 300$ m: (a) air parcel elevation (thin black) and ridge profile (thick gray); (b) temperature (thin black) and temperature under the assumption that θ is constant along the trajectory (thick gray); (c) actual along-gap wind component (thin black) and along-gap wind component under the assumptions that B and θ are conserved along the trajectory and that v and w are negligible (thick gray); (d) $B^* = B - c_p T_0$, the Bernoulli function minus the enthalpy of the parcel at the upstream end of the trajectory (thin black) and the constant B_0^* reference line (thick gray); and (e) potential temperature.

ilar magnitudes in all the simulations, the potential for the local amplification processes to generate damaging winds is greatest in the mountain wave regime.

Figure 12 shows the variation of several key parameters along a trajectory above the centerline of the gap in the $\epsilon = 1.4$ simulation. The trajectory lies along the line $y = 0$; the x coordinate of the parcel is labeled along the bottom axis. Figure 12a shows the elevation of the parcel, along with the cross section of the ridge. The parcel, which exits the gap (at $x = 40$ km) at a height of 300 m, originates from an elevation of roughly 870 m in the upstream flow, and ascends to 1239 m in the gap-entrance region. The adiabatic heating and cooling associated with these vertical motions is mirrored in the parcel temperature (Fig. 12b). Note that the temperature of the parcel increases by roughly 5 K as it moves along the trajectory. Despite the increase in enthalpy, the parcel accelerates from 6.4 m s^{-1} over the gap entrance to 21 m s^{-1} in the exit region because of the conversion of potential to kinetic energy during its 939-m descent (Fig. 12c). Because of this descent, there is an *increase* in atmospheric pressure along the trajectory between the gap-entrance and -exit regions. Thus if (11) were applied along the actual trajectory, instead of at constant height, it would erroneously predict that air parcels decelerate as they pass through the gap.

To what extent can the acceleration of the gap wind be predicted from Bernoulli's equation? As indicated in Figs. 12d and 12e, neither the Bernoulli function B nor the potential temperature are exactly conserved along the air parcel trajectory. The small increase in the potential temperature along the trajectory is due to the action of the fourth-order smoother on steep gradients in the numerically simulated potential temperature field. If the potential temperature data are adjusted to remove the effects of the fourth-order smoother, the simulated wind speed may be shown to be in very good agreement with that which would be predicted based on conservation of the Bernoulli function. To demonstrate such agreement, B and T were recomputed along the trajectory as if θ were exactly conserved, and the results were plotted as the thick gray curves in Figs. 12d and 12b. With θ held constant, B is constant along the trajectory (thick gray curve in Fig. 12d), yet there is essentially no change in the along-trajectory fluctuation in T shown in Fig. 12b. Finally, assuming a constant value for B, the variation in u along the trajectory was evaluated from the along-trajectory values of T and z and plotted as the thick gray curve in Fig. 12c. Comparing the actual variations in u along the trajectory (thin black curve) with those deduced from conservation of the Bernoulli function assuming adiabatic flow (thick gray curve), it

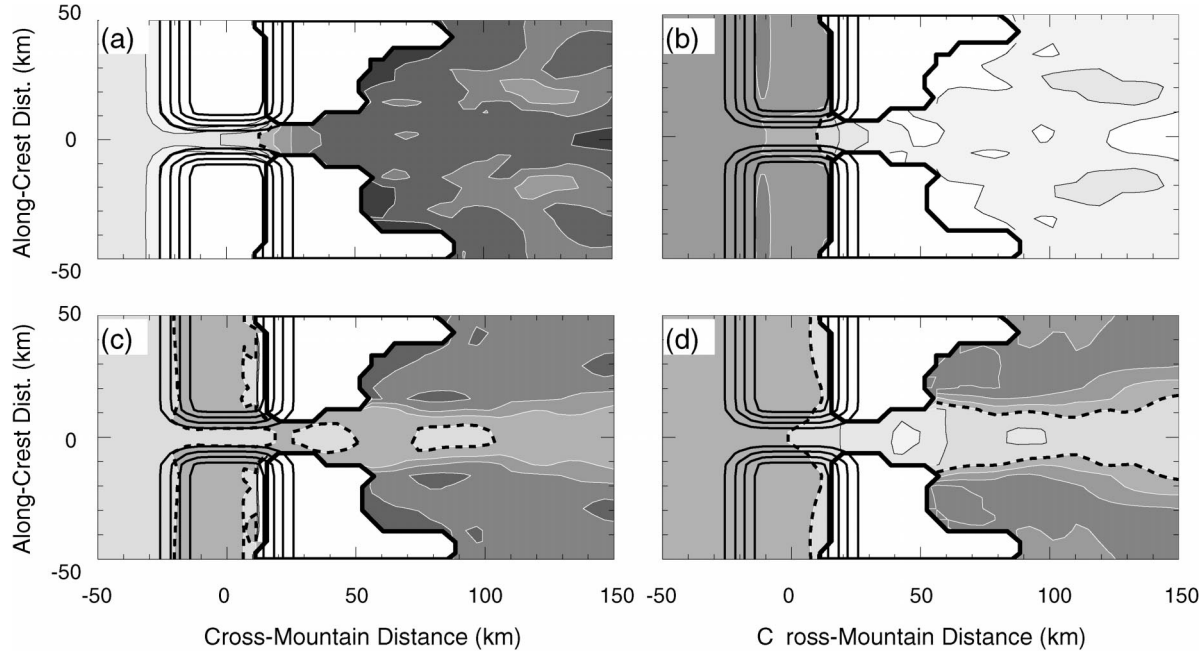

FIG. 13. Normalized perturbation fields on the $\theta = 276$ K surface (a) height $\tilde{z}$, (b) pressure $\tilde{\pi}$, (c) Bernoulli function $\overline{B}$, and (d) cross-mountain wind speed $\tilde{u}$. Light (dark) shading denotes positive (negative) perturbations; the zero contour is the heavy black and white dashed line. Contour intervals are (a) 0.2, (b) 0.01, (c) 0.01, and (d) 0.5. The thick black line denotes the area where the constant potential temperature surface intersects the ground.

is apparent the two are almost identical. Thus for this trajectory, which lies outside the wave-breaking region, the analysis of air parcel accelerations via Bernoulli's equation yields quantitatively correct results after compensating for the small impact of fourth-order smoothing on the potential temperature.

This same type of Bernoulli function analysis shows that descent continues to play a crucial role in producing acceleration along those trajectories that exit the gap very near the surface. In particular, an air parcel originating at $z = 283$ m upstream subsequently decelerates while rising to a height of 724 m in the gap-entrance region before finally accelerating as it descends to exit the gap at $z = 50$ m, the lowest level at which thermodynamic and horizontal wind data are carried in the numerical model.

7. Bernoulli function distribution in jets and wakes

Pan and Smith (1999) performed shallow-water simulations in which a uniform upstream flow encountered a long ridge pierced by a series of gaps. A gap-wind jet flanked by regions of decelerated flow was found over the level terrain in the lee of each gap. Since the Bernoulli function for the shallow-water flow over flat bottom topography is simply

$$B_{sw} = \frac{1}{2}\rho U^2 + \rho g H,$$

where U is the horizontal flow speed and H the fluid depth, Pan and Smith (1999) noted that the variations in B_{sw} depend solely on the variations in the horizontal speed of the fluid and the fluid depth. Furthermore, since the fluid depth tends to equilibrate downstream of the obstacle, they found that the variations in U^2 were directly proportional to the values of B_{sw} within the wake region. The gap-wind jet appeared in a region of relatively high B_{sw}; the slower winds within the wake on each side of the jet were associated with lower values of B_{sw}. This spatial gradient in B_{sw} was generated by dissipation and Bernoulli loss in jumps in the lee of the ridges on each side of the gap, whereas there was no dissipation or Bernoulli loss within the gap flow itself.

In the mountain wave regime ($\epsilon = 1.4$), which produces the strongest gap winds, there is no tendency for the gap-wind jet to coincide with a region of high Bernoulli function if both fields are compared on a constant level surface. If, however, these fields are plotted on an isentropic surface (which is a better analog to the free surface in a shallow-water model because for inviscid flow the isentropic surface is a material surface), the region of strong gap flow does indeed coincide with a region of high Bernoulli function, as shown in Figs. 13c and 13d. The normalized perturbation vertical displacement $\tilde{z} = (z - z_0)/z_0$ of the 276-K isentropic surface is plotted in Fig. 13a, where $z_0 = 1.14$ km is the undisturbed height of that isentropic surface in the upstream flow. The 276-K θ surface ascends so that $\tilde{z}$ increases

to roughly 1.4 throughout a broad region immediately upstream of the gap; the surface continues to ascend as it passes over the crest of the ridge, and then plunges to the ground along the lee slope on each side of the gap. Within the gap-exit jet itself, the 276-K θ surface never intersects the ground, but $\tilde{z}$ falls below 0.4. Not surprisingly, this descent is associated with an increase in the atmospheric pressure along the isentropic surface, which is shown in Fig. 13b by the field of normalized perturbation pressure $\tilde{\pi} = (\pi - \pi_0)/\pi_0$ (where π_0 is the value of the Exner-function pressure on the undisturbed 276-K surface).

As in the shallow-water case examined by Pan and Smith, the Bernoulli function in the region of the gap flow is essentially unmodified from its upstream value, whereas the lower values of the Bernoulli function throughout the remainder of the wake appear to have been produced by dissipation in the wave-breaking regions over and leeward of the higher topography. This is apparent in Fig. 13c, which shows contours of the normalized perturbation Bernoulli function $\tilde{B} = (B - B_0)/B_0$ (where B_0 is the Bernoulli function on the undisturbed 276-K isentropic surface). In fact, $\tilde{B}$ remains in the range $[-0.005, 0.005]$ along an air parcel trajectory through the gap, but $\tilde{B}$ drops below -0.03 downstream of the wave-breaking regions.

The normalized perturbation x component of the velocity $\tilde{u} = (u - u_0)/u_0$ (where u_0 is the value of u on the undisturbed 276-K θ surface) is plotted in Fig. 13d. Clearly high values of $\tilde{u}$ are found in the regions of highest $\tilde{B}$. Within the gap flow at $x = 45$ km plotted in Fig. 13c, $\tilde{u}$ exceeds 1.0, implying the wind speeds are more than double their value in the undisturbed flow. Farther downstream the winds decrease, but $\tilde{u}$ still remains positive, indicating air parcels have undergone net acceleration. These high winds are associated with a cross-wake maximum in $\tilde{B}$, but in contrast to the single-layer shallow-water results, the lee-side pressure on the isentropic surface is higher than the pressure upstream (see Fig. 13b). Indeed even within the wake, the pressure and the enthalpy are slightly higher along the jet axis [since the data are plotted on an isentropic surface, the perturbation enthalpy $c_p(T - T_0)$ is just $c_p\theta_0\pi_0\tilde{\pi}$, so its spatial distribution is identical to that for $\tilde{\pi}$]. Rather than a pressure minimum, the gap-wind jet downstream of $x = 100$ km is associated with a cross-wake minimum in $\tilde{z}$.

The results shown in Fig. 13 are consistent with those examined in more quantitative detail in Fig. 12 by following an air parcel trajectory that originated at the $\theta = 275.4$ K level along the centerline of the gap. Both θ and B are almost conserved along trajectories passing through the center of the gap-wind jet; the Bernoulli function is able to remain constant despite increases in both enthalpy and wind speed, because the air parcels undergo significant descent.

8. Conclusions

This paper has examined gap winds generated by an airstream with uniform static stability and horizontal wind speed impinging on an isolated ridge cut by a relatively narrow gap. Both the barrier-scale response and the flow within the gap itself have been investigated as a function of the normalized mountain height $\epsilon = Nh_0/U$.

On the scale of the entire barrier, the previously well documented transition from a flow-over regime for $\epsilon < O(1)$ to a flow-around regime for $\epsilon > O(1)$ was clearly evident in our numerical simulations. The fraction of the oncoming flow passing through the gap did not, however, reveal any such regime change. In comparison to the dramatic ϵ-dependent changes in the percentage of flow going over or around the ridge, the percentage of the total flow passing through the gap was found to be relatively independent of ϵ. This result, which was obtained for gaps that transmitted up to 40% of the oncoming low-level flow, must not be applicable to gaps that are so wide that the flow through the gap becomes indistinguishable from the flow around the interior end of each adjacent ridge. Unfortunately, limitations on our computational resources prevented us from determining the width at which the change to a flow-around regime begins to increase the proportion of air channeled through the gap.

The kinematics of the flow within the gap itself were investigated by examining mass budgets through three control volumes located in the entrance, central, and exit regions of the gap. Three basic gap-flow regimes were encountered for different ranges of ϵ. In the *linear regime*, which included the $\epsilon = 0.25$ case, there was almost no enhancement of the gap flow. The $\epsilon = 1.4$ case was representative of the *mountain wave regime*, in which there is a monotonic increase in the along-gap mass fluxes through all three control volumes and a particularly strong increase in the mass flux and wind speed within the exit volume due to downward transport by the mountain wave above the lee slopes of the topography. The *upstream-blocking regime* is well illustrated by the $\epsilon = 5.0$ case, in which the largest increase in the along-gap mass flux occurs in the entrance volume due to lateral convergence. In contrast to the mountain wave regime, in which the highest gap winds appear downstream near the exit, the highest winds occur in the upstream portion of the gap in the upstream-blocking regime.

The dynamical processes associated with each flow regime were determined by examining the momentum budgets for control volumes in the entrance, central, and exit regions. The momentum budgets confirm the crucial importance of vertical transport in creating the high winds in the gap-exit region in the mountain wave regime. On the other hand, vertical momentum transport plays almost no role in generating the high winds in the upstream-blocking regime, which are produced by lat-

eral momentum flux convergence and pressure gradient forces in the entrance volume.

In a previous study of airflow with constant N and U perpendicular to a ridge with a gap, Zängl (2002) identified two flow regimes, linear and nonlinear, and suggested that in the nonlinear regime confluence on the upstream side of the mountain is negligible and ''the low-level pressure difference across the mountain ridge primarily drives the gap flow.'' Zängl's topography rose to a single peak, rather than the flat-top ridge used in this study. As a consequence, the dynamical processes active at the gap-entrance and -exit regions are not easily separated in his results. His nonlinear regime is comparable to the mountain wave regime identified in this paper, although our Eulerian momentum budgets for flow in the mountain wave regime show that the pressure gradient force is not the single dominant factor accelerating the gap winds. We also found upstream confluence to be important for gap-wind acceleration in the upstream-blocking regime, but the prototypical examples of this type of flow occur at larger values of ϵ than the maximum of 3.0 considered by Zängl, so our findings are not inconsistent with his results.

In our simulations, the variations in ϵ were obtained by holding h_0 and N fixed while varying U. To the extent that a constant N and U profile may be offered as a model for the real atmosphere, the strategy of varying ϵ by changing U mimics the situation involving airflow across a given mountain barrier in the real world. The mountain height is obviously fixed, and the tropospheric static stability averaged through a *deep* layer is never greatly different from 0.01 s^{-1}. The primary variations in the deep-layer-averaged ϵ are due to changes in the cross-mountain wind speed.

Since the gap winds that develop in the upstream-blocking regime involve accelerations with respect to a weak mean flow, the upstream-blocking regime is not likely to be associated with damaging winds in real-world applications (2.8 m s^{-1} winds upstream accelerate to 7 m s^{-1} in the gap in the $\epsilon = 5.0$ case). The mountain wave regime appears far more likely to serve as a model for those severe gap winds that develop in response to strong cross-mountain flow in real-world events. Indeed, previous work by Colman and Dierking (1992) and Colle and Mass (1998b) has suggested that mountain waves play a major role in enhancing gap winds along the Taku River in Alaska and through the Stampede Gap in Washington State.

The dynamics of potentially severe gap winds produced in the mountain wave regime were further investigated by evaluating the Bernoulli function along air parcel trajectories for the $\epsilon = 1.4$ simulation. Complementing the control-volume budgets for mass and momentum, the trajectory analysis confirmed the link between descent and acceleration in the gap flow, even for parcels exiting the gap at heights as low as 50 m.

Previous attempts to diagnose the strength of gap winds using Bernoulli's equation for an incompressible fluid under the assumption of level flow (11) have typically led to serious overprediction of the wind speed. However, (11) is defective because it neglects the influence of changes in atmospheric density. The correct expression for conservation of the Bernoulli function for level flow in a compressible atmosphere is (12), which implies that constant-level gap winds will undergo acceleration only if the temperature at the gap exit is *lower* than the temperature at the gap entrance. Observations often show higher temperatures at the exit than at the entrance during gap-flow events, and this is also the case in the $\epsilon = 1.4$ simulation. Gap-wind acceleration is sustained despite the increase in temperature between the entrance and the exit because the air parcels undergo net descent during their passage through the gap.

Comparison of the Bernoulli function distribution on an isentropic surface in the high-wind $\epsilon = 1.4$ case shows similarities to the shallow-water results obtained by Pan and Smith (1999) in that the regions of highest Bernoulli function are coincident with the highest gap winds, and the B field is essentially unmodified within the gap-exit jet but is reduced on each side of the jet by dissipation in the wave-breaking regions in the lee of the higher topography. The flow undergoes substantial subsidence as it accelerates near the gap exit to more than double the speed of the upstream winds. It is this subsidence, rather than the change in pressure (which increases along the isentropic trajectory) that gives the most direct analog to the downward free-surface displacements in the Bernoulli equation analysis of shallow-water gap flow.

Surface friction is a potentially important factor limiting the maximum velocities in actual gap-wind events. The influence of surface friction together with the impact of pressure-driven channeling associated with geostrophic flows crossing the ridge at various angles will be investigated in Part II of this paper. In Part II, it will be demonstrated that these additional factors do not change the central conclusion of this paper, that at least in the mountain wave regime, vertical fluxes of momentum and mass play a crucial role in the formation of strong gap winds.

Acknowledgments. This research was supported by National Science Foundation Grants ATM-9817728 and ATM-0137335.

REFERENCES

Baines, P. G., 1979: Observations of stratified flow past three-dimensional barriers. *J. Geophys. Res.*, **84,** 7834–7838.

——, 1995: *Topographic Effects in Stratified Flows.* Cambridge University Press, 496 pp.

Bougeault, P., 1983: A nonreflective upper boundary condition for limited-height hydrostatic models. *Mon. Wea. Rev.*, **111,** 420–429.

Colle, B. A., and C. F. Mass, 1998a: Windstorms along the western side of the Washington Cascade Mountains. Part I: A high-res-

olution observational and modeling study of the 12 February 1995 event. *Mon. Wea. Rev.*, **126,** 28–52.
——, and ——, 1998b: Windstorms along the western side of the Washington Cascade Mountains. Part II: Characteristics of past events and three-dimensional idealized simulations. *Mon. Wea. Rev.*, **126,** 53–71.
——, and ——, 2000: High-resolution observations and numerical simulations of easterly gap flow through the Strait of Juan de Fuca on 9–10 December 1995. *Mon. Wea. Rev.*, **128,** 2398–2422.
Colman, B. R., and C. F. Dierking, 1992: The Taku wind of southeast Alaska: Its identification and prediction. *Wea. Forecasting*, **7,** 49–64.
Dorman, C. E., R. C. Beardsley, and R. Limeburner, 1995: Winds in the Strait of Gibraltar. *Quart. J. Roy. Meteor. Soc.*, **121,** 1903–1921.
Durran, D. R., 1999: *Numerical Methods for Wave Equations in Geophysical Fluid Dynamics.* Springer-Verlag, 465 pp.
——, and J. B. Klemp, 1983: A compressible model for the simulation of moist mountain waves. *Mon. Wea. Rev.*, **111,** 2341–2361.
Epifanio, C. C., and D. R. Durran, 2001: Three-dimensional effects in high-drag-state flows over long ridges. *J. Atmos. Sci.*, **58,** 1051–1065.
Gal-Chen, T., and R. Sommerville, 1975: On the use of a coordinate transformation for the solution of the Navier–Stokes equations. *J. Comput. Phys.*, **17,** 209–228.
Jackson, P. L., and D. Steyn, 1994a: Gap winds in a fjord. Part I: Observations and numerical simulations. *Mon. Wea. Rev.*, **122,** 2645–2665.
——, and ——, 1994b: Gap winds in a fjord. Part II: Hydraulic analog. *Mon. Wea. Rev.*, **122,** 2666–2676.
Klemp, J. B., and D. Durran, 1983: An upper boundary condition permitting internal gravity wave radiation in numerical mesoscale models. *Mon. Wea. Rev.*, **111,** 430–444.
Lackmann, G. M., and J. E. Overland, 1989: Atmospheric structure and momentum balance during a gap-wind event in Shelikof Strait, Alaska. *Mon. Wea. Rev.*, **117,** 1817–1833.
Lilly, D. K., 1962: On the numerical simulation of buoyant convection. *Tellus*, **14,** 148–172.
Mass, C. F., S. Businger, M. D. Albright, and Z. A. Tucker, 1995: A windstorm in the lee of a gap in a coastal mountain barrier. *Mon. Wea. Rev.*, **123,** 315–331.
Ólafsson, H., and P. Bougeault, 1997: The effect of rotation and surface friction on orographic drag. *J. Atmos. Sci.*, **54,** 193–210.
Overland, J., 1984: Scale analysis of marine winds in straits and along mountain coasts. *Mon. Wea. Rev.*, **112,** 2530–2534.
Pan, F., and R. B. Smith, 1999: Gap winds and wakes: SAR observations and numerical simulations. *J. Atmos. Sci.*, **56,** 905–923.
Reed, R. J., 1981: A case study of a Bora-like windstorm in western Washington. *Mon. Wea. Rev.*, **109,** 2383–2393.
Saito, K., 1993: A numerical study of the local downslope wind ''Yamaji-kaze'' in Japan. Part 2: Non-linear aspect of the 3-d flow over a mountain range with a col. *J. Meteor. Soc. Japan*, **71,** 247–271.
Scorer, R., 1952: Mountain-gap winds; a study of surface wind at Gibraltar. *Quart. J. Roy. Meteor. Soc.*, **78,** 53–61.
Skamarock, W. C., and J. B. Klemp, 1993: Adaptive grid refinement for two-dimensional and three-dimensional nonhydrostatic atmospheric flow. *Mon. Wea. Rev.*, **121,** 788–804.
Smedman, A.-S., H. Bergström, and U. Högström, 1996: Measured and modelled local wind fields over a frozen lake in a mountainous area. *Beitr. Phys. Atmos.*, **69,** 501–516.
Smith, R. B., 1989: Mountain induced stagnation points in hydrostatic flow. *Tellus*, **41A,** 270–274.
Steenburgh, J. W., D. M. Schultz, and B. A. Colle, 1998: The structure and evolution of gap outflow over the Gulf of Tehuantepec, Mexico. *Mon. Wea. Rev.*, **126,** 2673–2691.
Whiteman, C. D., and J. C. Doran, 1993: The relationship between overlying synoptic-scale flows and winds within a valley. *J. Appl. Meteor.*, **32,** 1669–1682.
Zängl, G., 2002: Stratified flow over a mountain with a gap: Linear theory and numerical simulations. *Quart. J. Roy. Meteor. Soc.*, **128,** 927–949.